JOURNAL OF GUIDANCE, CONTROL, AND DYNAMICS
Vol. 23, No. 6, November–December 2000

Fundamental Aeroservoelastic Study Combining Unsteady Computational Fluid Mechanics with Adaptive Control

Damien M. Guillot* and Peretz P. Friedmann†
University of California, Los Angeles, California 90025-1597

A computational two-dimensional aeroservoelastic study in the time domain is described. The model, which is based on exact inviscid aerodynamics, captures the large amplitude motions and the associated strong shock dynamics in the transonic regime. The aeroservoelastic system consists of a two-degree-of-freedom airfoil with a trailing-edge control surface. By the use of first-order actuator dynamics, a digital adaptive controller is applied to provide active flutter suppression. Comparisons between time responses of the open-loop and closed-loop systems show the ability of the trailing-edge control surface to suppress nonlinear transonic aeroelastic phenomena. A relation between actuator dynamics, sampling time step, and limits on the flap deflection angle to guarantee the effectiveness of the adaptive controller is illustrated by the results.

Nomenclature

a_h	=	nondimensional elastic axis location, measured from midchord
a_∞	=	freestream speed of sound
b	=	airfoil semichord
C_h	=	hinge moment coefficient
C_l, C_m	=	lift and moment coefficients about the elastic axis, respectively
Cp	=	pressure coefficient $(p - p_\infty)/(1/2\rho_\infty U_\infty^2)$
c	=	chord
c_β	=	nondimensional flap hinge axis location, measured from midchord
$\{D_i\}$	=	artificial dissipation vector at node i
h	=	plunge displacement
I_α	=	moment of inertia of the airfoil with flap in neutral position, about the elastic axis
I_β	=	flap moment of inertia about the hinge axis
J	=	performance index
K	=	reduced frequency, $\omega b/U_\infty$
K_h, K_α, K_β	=	springs constants, for the springs restraining bending, plunging, and flap rotation
M	=	Mach number
$[M]$, $[K]$	=	mass and stiffness matrices for the three-degree-of-freedom (3-DOF) airfoil section
m	=	airfoil mass
N_n	=	number of nodes in the mesh surrounding the airfoil
p	=	pressure
$[Q]$	=	positive semidefinite symmetric matrix
$\{Q_i\}$	=	flux vector at node i
r_w	=	positive weighting coefficient
r_α	=	radius of gyration of the airfoil about the elastic axis $[I_\alpha/(mb^2)]^{1/2}$
r_β	=	radius of gyration of the flap about the hinge axis $[I_\beta/(mb^2)]^{1/2}$
S_α	=	static moment of the airfoil with flap in neutral position, about the elastic axis
S_β	=	flap static moment, about the hinge axis
Te	=	sampling time step for parameter estimator
t	=	time
$\bar{U}$	=	nondimensional speed, $U_m/(b\omega_\alpha)$
u, v	=	Cartesian velocity components of the fluid
$\{w_i\}$	=	flow vector at node i
$\{w_{ST}\}$	=	structural state vector $\{\{q\}^T, \{\dot{q}\}^T\}^T$
$\{X_p\}$	=	state vector of the estimated deterministic autoregressive moving average (ARMA) model
x_α	=	nondimensional static moment of the airfoil with flap in neutral position, about the elastic axis, also equal to the static unbalance, nondimensionalized with respect to the semichord b, $S_\alpha/(mb)$
x_β	=	nondimensional flap static moment about the hinge axis, $S_\beta/(mb)$
y	=	output of the ARMA model
α	=	airfoil angle of attack
β	=	flap deflection angle
$\beta_{\max}$	=	maximum commanded flap deflection angle
γ	=	ratio of specific heats
δ_h	=	hinge moment correction factor
μ	=	mass ratio, $m/(\pi\rho_\infty b^2)$
ξ	=	nondimensional plunge displacement, h/b
ρ	=	air density
ω_h, ω_α, ω_β	=	uncoupled natural frequencies associated with the three respective DOF's $(K_h/m)^{1/2}$, $(K_\alpha/I_\alpha)^{1/2}$, and $(K_\beta/I_\beta)^{1/2}$, respectively

Special Symbols

k	=	values at estimation time $k \times Te$, subscript
T	=	transpose operator, superscript
∞	=	freestream values, subscript

Introduction

INTERACTION between structural dynamics, aerodynamics, and flight control systems, namely, aeroservoelasticity, has received considerable attention during the last two decades, leading to the development of active control technology (ACT). Extensive research has been carried out on ACT concepts, such as gust alleviation and active flutter suppression. A survey of research in this field has been presented by Noll;[1] however, as indicated by a recent review article by Friedmann,[2] active flutter suppression systems are not implemented in production aircraft.

Until the mid-1980s, lack of efficient computational tools restricted the study of aeroservoelastic systems to linear subsonic and supersonic flight regimes. Since then, progress in computational fluid dynamics (CFD) has led to accurate computations of two-dimensional and three-dimensional unsteady transonic aerodynamic loads for viscous and inviscid flows in the time domain. However, because numerous simulations based on the direct integration of the aerodynamic equations in the time domain must be performed to carry out any aeroservoelastic study, theoretical aeroelastic studies

Received 2 August 1999; revision received 20 April 2000; accepted for publication 21 April 2000.

*Visiting Scholar, Mechanical and Aerospace Engineering Department; currently Research Engineer Aerospatiale, Toulon, France.

†Professor, Mechanical and Aerospace Engineering Department; currently François-Xavier Bagnoud Professor, Department of Aerospace Engineering, University of Michigan, Ann Arbor, MI 48109. Fellow AIAA.

combining control surfaces with a CFD approach have relied primarily on solution of the transonic small disturbance equation[3–5] and the full potential equation.[6–8] In these studies, the representation of the controller was fairly simple, and either velocity or acceleration feedback was used.

Guruswamy and Tu[9] pointed out that the combined effect of the shock wave and flow discontinuity due to the presence of the control surface hinge can significantly influence both the aerodynamic and aeroelastic behavior of the wing. Using a simple control law, where the flap deflection angle was proportional to the angle of attack, they found that in the high transonic regime, when shock waves moved aft of the hinge axis, the active control surface became ineffective. Studies on an F5 wing[10] produced similar results, which implies that control laws that fail to account for strong interactions between the fluid and the structure may be ineffective in the transonic regime. The importance of simultaneous integration of structures, aerodynamics, and active controls in the transonic domain is clearly emphasized by this concise review, as well as by the more comprehensive reviews presented in Refs. 1 and 2.

Recently, aeroelastic studies based on the Euler equations were carried out, and efficient computational codes have been developed and applied to the study of two-dimensional and three-dimensional problems.[11–14] The use of Euler equations allowed studies of transonic flows with strong shock waves, where nonlinear phenomena, such as weak divergence and limit cycle flutter, can occur. The role of shock dynamics in transonic flutter was clarified by Bendiksen.[15] Again, note that viscosity was neglected in Refs. 11–15.

In another study, a digital adaptive controller was applied to the active time-varying flight conditions in subsonic and transonic flows.[16] The controller was found to be robust and efficient under both random external loads and time-varying conditions. The aerodynamic loads were computed by approximating the three-dimensional unsteady transonic aerodynamic loads in the time domain for time-varying freestream Mach numbers. Although the transonic bucket effect was effectively captured by this method, the ability of the approximation to capture unsteady aerodynamic effects was marginal.

The present study is motivated by the desire to model in a more comprehensive manner the strong fluid–structure coupling and determine its influence on control law design in transonic flow. Clearly, the use of the Euler equations prevents us from modeling shock wave/boundary layer interaction. However, such effects are beyond the scope of the present study, which focuses on the application of an adaptive controller to flutter suppression in transonic flow. The specific objectives of the present paper are 1) efficient computation of the inviscid unsteady flow about a two-dimensional airfoil/trailing-edge control surface combination; 2) detailed study of the open-loop aeroservoelastic system to determine its flutter boundary, nonlinear flutter, and divergence in the time domain; 3) study of flutter suppression using an adaptive controller, which was found to be quite successful for weakly nonlinear systems[16]; and 4) study of other aspects of the problem such as actuator dynamics.

The numerical results presented in the paper illustrate some interesting aspects of transonic flutter suppression in the presence of shock waves and aerodynamic nonlinearities.

Formulation of the Aeroservoelastic Model and Method of Solution

Aeroservoelastic Model

The aeroelasic model, shown in Fig. 1, consists of a typical cross section of a wing having plunge and pitch degrees of freedom, combined with a trailing-edge control surface representing an actively controlled flap. In practice, there is a gap between the flap and the airfoil. Correct treatment of the flow in the gap requires the treatment of viscous effects. Because the viscous effects are excluded from this study, the actual physical gap due to the flap is also eliminated.

The kinetic energy of the three-degree-of-freedom (3-DOF) system has the following form:

$$T = \tfrac{1}{2} m b^2 \{\dot{q}\}^T [M] \{\dot{q}\} \tag{1}$$

Where

$$\{q\}^T = \lfloor \zeta \quad \alpha \quad \beta \rfloor \tag{2}$$

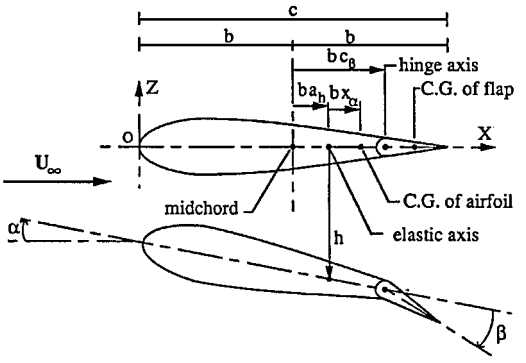

Fig. 1 Definition of parameters for 3-DOF aeroservoelastic model.

$$[M] = \begin{bmatrix} 1 & x_\alpha & x_\beta \\ x_\alpha & r_\alpha^2 & r_\beta^2 + x_\beta(c_\beta - a_h) \\ x_\beta & r_\beta^2 + x_\beta(c_\beta - a_h) & r_\beta^2 \end{bmatrix} \tag{3}$$

As in Ref. 17, the displacements of the airfoil are restrained by elastic springs: a linear spring located at the elastic axis restrains the bending h, a torsional spring located at the same axis restrains the pitching α, and the flap rotation β is restrained by a torsional spring at the flap hinge axis. These spring stiffnesses are representative of the structural stiffnesses of the system. Therefore, the strain energy of the 3-DOF airfoil section has the following expression:

$$U = \tfrac{1}{2} K_h h^2 + \tfrac{1}{2} K_\alpha \alpha^2 + \tfrac{1}{2} K_\beta \beta^2 \tag{4}$$

Expressing the spring constants in terms of uncoupled natural frequencies ω_h, ω_α, and ω_β, the strain energy can be written as follows:

$$U = \tfrac{1}{2} m b^2 \omega_\alpha^2 \{q\}^T [K] \{q\} \tag{5}$$

with

$$[K] = \begin{bmatrix} (\omega_h/\omega_\alpha)^2 & 0 & 0 \\ 0 & r_\alpha^2 & 0 \\ 0 & 0 & (\omega_\beta/\omega_\alpha)^2 r_\beta^2 \end{bmatrix} \tag{6}$$

Neglecting structural damping and using the previous nondimensional expressions of the kinetic and strain energies together with Lagrange equations yields the equations of motion for this 3-DOF aeroelastic system:

$$[M]\{\ddot{q}\} + \omega_\alpha^2 [K]\{q\} = \begin{Bmatrix} -C_\ell \\ 2C_m \\ 2C_h \end{Bmatrix} \tag{7}$$

where the right-hand side of Eq. (7) represents the nondimensional generalized aerodynamic load.

The aerodynamic coefficients are computed by integrating the pressure distribution around the airfoil. Unsteady flow calculations have shown that trailing-edge control surface pressure distribution and hinge moment coefficients are generally overestimated when viscous effects are neglected. Moreover, the gap between the control surface and the wing is not considered in this study. A constant hinge moment correction factor δ_h based on empirical information is introduced to test the effectiveness of the active controller with respect to hinge moment coefficients.

Integration of Aerodynamic and Structural Equations

The unsteady solution of the Euler equations is based on a finite element approach developed by Bendiksen[18] and Davis and Bendiksen,[19] where aerodynamic and structural equations are written in the same form and, thus, can be solved simultaneously by the same time-marching algorithm. This approach is capable of capturing the effect of shocks, which are known to be significant.[20,21]

The spatial discretization of the aerodynamic equations leads to the following set of vector equations for the two-dimensional case, written for each node i of the mesh:

$$\frac{\mathrm{d}}{\mathrm{d}t} \sum_{j=1}^{N_n} [m]_{ij} \{w_j\} + \{Q_i\} - \{D_i\} = 0 \tag{8}$$

where $[[m]_{ij}]_{ij=1,N_n}$ and $[\{Q_1\}^T, \ldots, \{Q_{N_n}\}^T]^T$ are the global consistent mass matrix and the global flux vector of the mesh surrounding the airfoil. The quantity $\{w_j\}$ is the vector of flow variables (density, Cartesian momentum components, total energy) at node j and $\{D_i\}$ represents an artificial dissipation term at node i, added to damp out numerical oscillations without adding mass, momentum, or energy to the system. Because of the coupling present in the consistent mass matrix, the aerodynamic equations are not in explicit form. To simplify the solution procedure, a diagonalized lumped mass matrix $[[m_L]_{ii}]$ is used; the cases studied in Ref. 19 show that the use of the consistent mass formulation did not provide an enhanced solution over the lumped mass approach.

The second-order linear differential equation for the aeroservoelastic system, Eq. (7), is transformed into a first-order state variable equation, similar to Eq. (8):

$$\frac{\mathrm{d}}{\mathrm{d}t}([M_{\mathrm{ST}}]\{w_{\mathrm{ST}}\}) + \omega_\alpha^2[K_{\mathrm{ST}}]\{w_{\mathrm{ST}}\} = \omega_\alpha^2 \frac{\bar{U}^2}{\pi\mu}\{R_{\mathrm{ST}}\} \tag{9}$$

where

$$\{w_{\mathrm{ST}}\} = \begin{Bmatrix} \{q\} \\ \{\dot{q}\} \end{Bmatrix} \tag{10}$$

$$[M_{\mathrm{ST}}] = \begin{bmatrix} \omega_\alpha^2[I] & [0] \\ [0] & [M] \end{bmatrix} \tag{11}$$

$$[K_{\mathrm{ST}}] = \begin{bmatrix} [0] & -[I] \\ [K] & [0] \end{bmatrix} \tag{12}$$

$$\{R_{\mathrm{ST}}\} = [0 \quad 0 \quad 0 \quad -C_l \quad 2C_m \quad 2C_h]^T \tag{13}$$

The near-field boundary condition consists of the requirement of flow tangency at the airfoil surface. It is implemented through the expressions for the flux terms.[19]

In the far field, a characteristic analysis based on Riemann invariants is used to determine the values of the flow variables on the exterior boundary of the mesh. This analysis is described by Jameson et al.,[22] Jameson and Baker,[23] Jameson and Schmidt,[24] and Jameson and Mavriplis[25] and was also used in Refs. 26 and 27. It correctly accounts for wave propagation in the far field, which is important for rapid convergence to steady state and serves as a nonreflecting boundary condition for unsteady applications.

A five-stage Runge–Kutta scheme is used to integrate the space-discretized system of the nonlinear equations (8) and (9) in time. For computational efficiency, the dissipative terms are evaluated only during the first two stages and frozen for the remaining three, as first suggested in Ref. 22. This scheme is a good compromise between computational efficiency (only two dissipative terms are evaluated) and high-frequency damping properties. It is superior to cases when the dissipative part is evaluated only once. Coefficients for this scheme that provide good stability characteristics are[24]:

$$\alpha_1 = \tfrac{1}{4}, \qquad \alpha_2 = \tfrac{1}{6}, \qquad \alpha_3 = \tfrac{3}{8}, \qquad \alpha_5 = 1 \tag{14}$$

These values were successfully used in Refs. 15, 18, and 19 for both steady and unsteady calculations and, therefore, they are also used in our study.

To maintain the mesh accuracy while the airfoil is moving, a boundary-fitted dynamic computational mesh algorithm should be capable of conforming continuously to the instantaneous position of the airfoil, while preserving the smoothness of the original mesh.

In Ref. 19, the mesh is deformed smoothly from zero at the far-field boundary of the values dictated by the airfoil pitch and plunge motions at the fluid–structure boundary. The node displacements are equal to the displacements computed under the assumption that the mesh is attached to the airfoil as a rigid body, multiplied by time-independent scale factors. These scale factors vary linearly with distance from the airfoil, ranging from unity at the airfoil surface to zero at the outer boundary. This method is quite simple to implement and deforms the mesh in a very smooth way. In the present study, flap motion prevents one from assuming that the airfoil is a rigid body. Therefore, substantial modifications of the mesh deformation scheme are required to account for the presence of the control surface.

The modified new approach is based on the sequential application of two methods. First, the approach given in Ref. 19 is used to compute the position of the nodes as dictated by the instantaneous position in pitch and plunge of the airfoil, with undeflected flap. Then nodes belonging to the flap are rotated around the hinge axis by the instantaneous flap deflection angle, which causes a significant deformation of the elements surrounding the flap. Assuming a flap deflection of about 1 deg and the hinge axis at 75% of the chord, the vertical displacement of the node at the trailing edge will be about $0.01b$, which is approximately the typical distance between two nodes in the region of the trailing edge. Therefore, nodes in this area have to be moved. This is done using a deformation scheme similar to Batina's.[26,28] A submesh surrounding the trailing edge is defined, for which nodes are moved. The submesh used in this study consists of the nodes that are less than half a chord from the trailing edge in the original mesh, where pitch, plunge, and flap displacements are zero. The mesh is modeled as a spring network, where each edge of each cell represents a linear spring. The spring stiffness is taken to be inversely proportional to the original length of the edge. Then the displacements of the submesh nodes are computed by writing the static equilibrium equations at each node and by solving the system using Jacobi or successive overrelaxation (SOR) iterations. The iterations are initialized by the displacement of the submesh nodes at the preceding step (predictor–corrector procedure). Because of the predictor step, it has been found that only one iteration is required to accurately move the mesh using SOR iterations.

Furthermore, to facilitate this method for the integration of aerodynamic and structural equations and make it suitable for aeroservoelastic applications, a significant effort was made to improve the numerical efficiency of the FORTRAN code. This consisted of vectorizing the code that reduced the CPU times by significant amounts.

Implementation of the Adaptive Control Law

In Ref. 16, a single-input/single-output deterministic autoregressive moving-average (ARMA) model, with $2M$ autoregressive and $2M$ moving-average coefficients was used to describe the input–output relation for the aeroservoelastic system. The unknown system coefficients were estimated using an on-line recursive estimation method, the Bierman's U-D method algorithm. The output consisted of the acceleration or the displacement measured at a point on the airfoil surface and filtered by an antialiasing filter, and the input was the optimal flap deflection angle, limited to a maximum amplitude $\beta_{\max}$ equal to 4 deg, unless otherwise specified. A detailed description of this approach can be found in Ref. 16.

Simple actuator dynamics, where the flap rotation speed is assumed to be perfectly controlled, will be considered first. In this case, flap inertia effects are neglected in the aeroservoelastic model. Subsequently, more realistic actuator dynamics will be taken into account to ensure practical feasibility of an effective active flutter suppression system.

An on-line adaptive control law was designed to minimize a linear quadratic performance index, given by

$$J = \sum_{k=0}^{\infty} \left(\{X_p\}_k^T [Q] \{X_p\}_k + r_w \beta_k^2 \right) \tag{15}$$

where $\{x_p\}_k$ is the state vector of the ARMA model at time $t = kTe$.

Results and Discussion

Calculations presented in this paper were carried out for NACA 0012 and NACA 64A006 airfoils, using grids derived from a structured quadrilateral cell Q mesh. Both mesh configurations consisted of 4092 node points of which 126 were on the airfoil surface and 128 were on the far-field boundary, which is set at a radius of 25 chords. A partial view of the NACA 0012 mesh is shown in Fig. 2. The same mesh is shown in Fig. 3 in the deformed state at a nose up pitch angle of 10 deg, a plunge displacement of $-0.02b$, and a positive flap deflection angle of 10 deg.

Verification of the Fluid/Structure Integration Scheme

Steady and unsteady flow computations were carried out and compared to previously published results. Figure 4 presents the steady pressure coefficients of a NACA 0012 at $M = 0.80$. Figure 5 shows the unsteady pressure coefficients for the upper and lower surface of a NACA 0012 pitching about the semichord at $M = 0.80$. The results shown in Figs. 4 and 5 represent our calculations, which are in very close numerical agreement with the results given in Ref. 19, which are not shown in Figs. 4 and 5. Note, however, that there are no significant differences between the two sets of results, and note

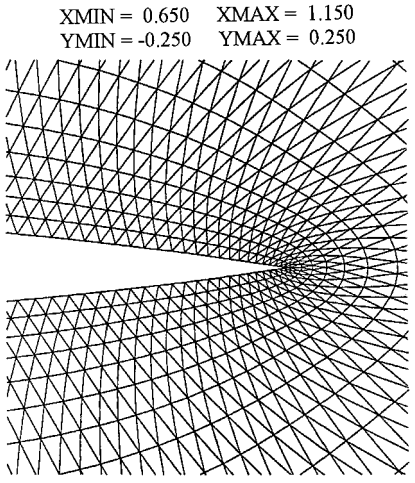

Fig. 2 Partial view of undeformed grid about NACA 0012 airfoil.

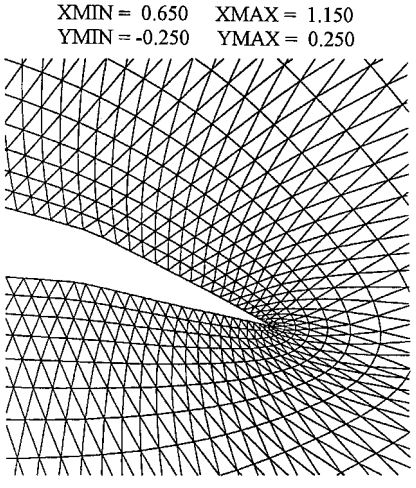

Fig. 3 Partial view of deformed grid about NACA 0012 airfoil (α = 10 deg, $h = -0.02b$, and β = 10 deg).

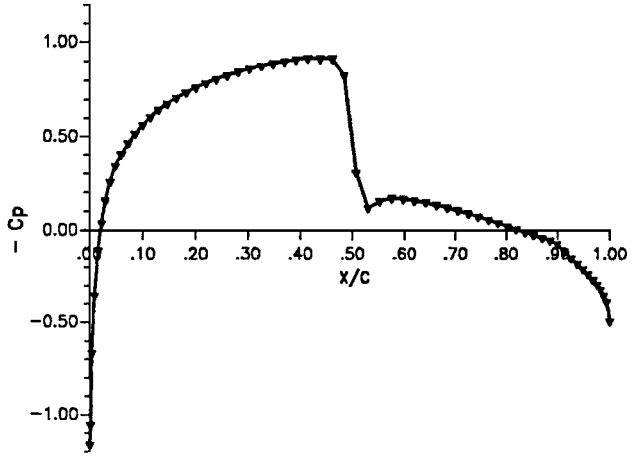

Fig. 4 Steady flow pressure coefficients for the NACA 0012 airfoil (M = 0.80).

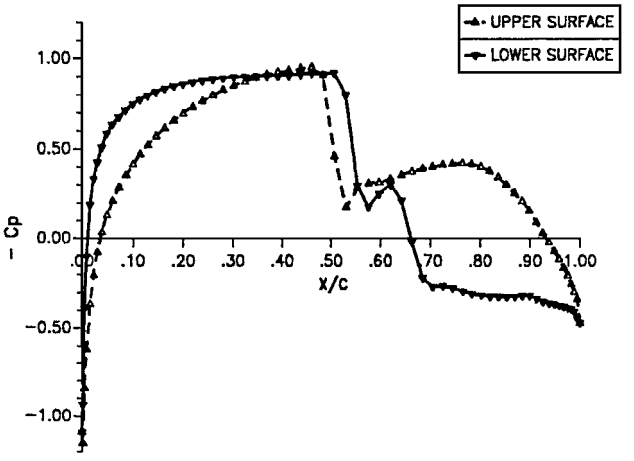

Fig. 5 Pressure coefficients for the NACA 0012 airfoil, at the beginning of the fifth cycle of forced pitching oscillations about $c/4$ (M = 0.80, K = 1.0, and α = 5.0 deg sin ωt).

that our results required considerably less CPU time per time step than used in Ref. 19, due to code parallelization.

The integration procedure in the presence of flap rotation is validated by the results displayed in Fig. 6, where our results are compared with those obtained in Refs. 27 and 29 for the NACA 64A006 airfoil with an oscillating flap at $M = 0.854$.

Open-Loop Studies

Aeroelastic response calculations for 2-DOF airfoils were carried out first. Two typical section wing models were considered. The first model is the NACA 64A006 typical section studied by Ashley[20] and by Kousen and Bendiksen[12] and Bendiksen.[15,18] In the present notation, it is described by the following nondimensional parameters:

$$a_h = -0.2, \qquad x_\alpha = 0.2, \qquad r_\alpha^2 = 0.29 (r_\alpha \simeq 0.5385)$$
$$\omega_h / \omega_\alpha = 0.3434$$

The second model is the NACA 0012 Benchmark Model, tested experimentally at the NASA Langley Research Center[21] and studied in Ref. 15. The nondimensional parameter values describing this configuration are

$$a_h = 0.0, \qquad x_\alpha = 0.0, \qquad r_\alpha^2 = 0.25, \qquad \omega_h / \omega_\alpha = 0.6564$$

For both models, calculations were performed at several values of Mach number, μ, and $\bar{U}$. Results obtained were found similar to those described in Refs. 11, 12, and 15. Typical results consist of limit cycle flutter and weak divergence phenomena, which are depicted in Figs. 7–9.

Subsequently, the open-loop 3-DOF system was studied and results were compared to those obtained in Ref. 3 using transonic small disturbance theory. In Ref. 3, a flutter sensitivity analysis of the 3-DOF NACA 64A006 airfoil was performed. Figure 10 shows the effect of Mach number on flutter speed for the $\mu = 50$ and the following parameter values:

$$a_h = 0.2, \qquad x_\alpha = 0.2, \qquad r_\alpha = 0.55, \qquad \omega_h / \omega_\alpha = 0.3$$

Here, $c_\beta = 0.5$ (hinge axis at $\frac{1}{4}$ of the trailing edge)

$$x_\beta = 0.008, \qquad r_\beta = 0.06, \qquad \omega_\beta / \omega_\alpha = 1.5$$

Figure 10 depicts the comparison of our results with those generated in Ref. 3. The difference in flutter speeds was found to be 3% at most. The flutter boundary, using the present time-domain model, was obtained by examining the time histories and determining those for which the response was stable and those for which it was unstable for several Mach numbers. The error in the flutter boundary obtained in this manner is less than 1%, which implies that for every Mach number selected, stable and unstable values were found within less than 1% of the estimated flutter speed. The initial conditions for the time-response calculations were the steady-state values of the flow variables and $(\mathrm{d}h/\mathrm{d}t)_0 = -0.01 c \omega_\alpha$. The flutter boundary of the airfoil with an undeflected flap and $\omega_\beta / \omega_\alpha = \infty$ (2-DOF airfoil),

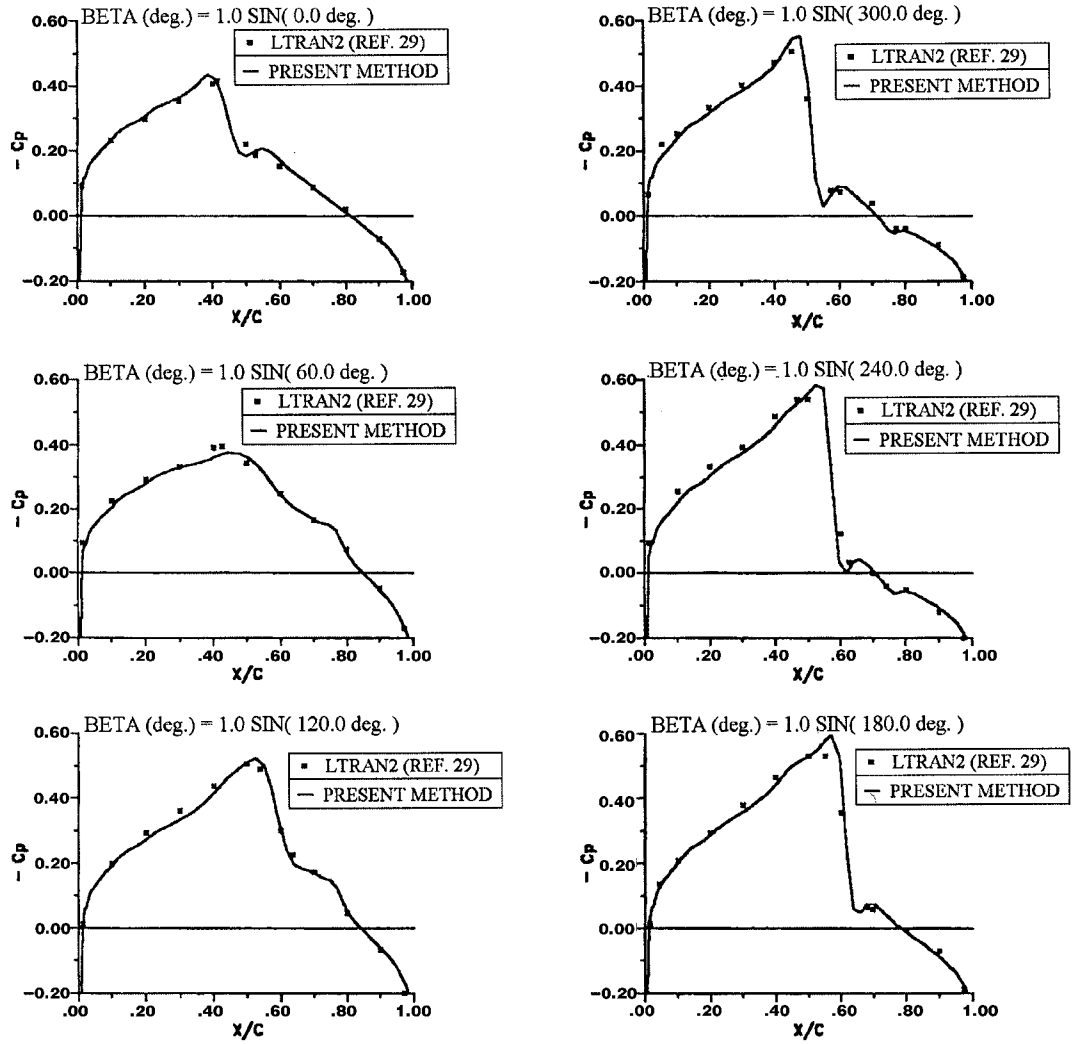

Fig. 6 Unsteady upper pressure coefficients for the NACA 64A006 airfoil, with an oscillating trailing-edge flap ($M = 0.854, k = 0.179$, and $\beta = 1.0$ deg sin ωt).

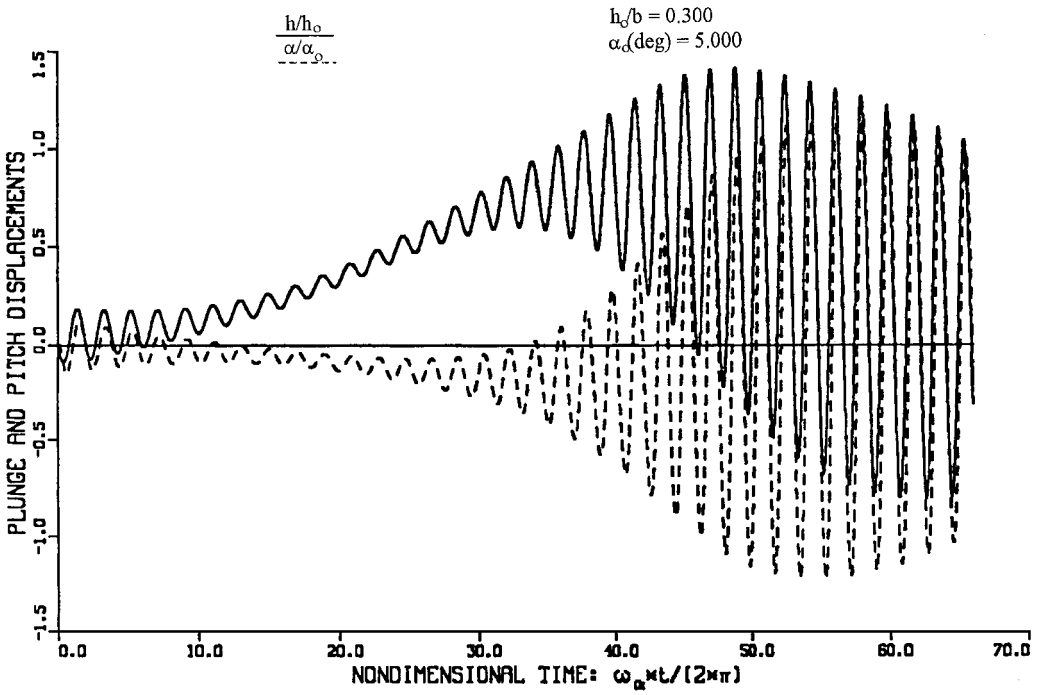

Fig. 7 Weak divergence and flutter–divergence interaction for the NACA 64A006 airfoil without flap and with initial pulse excitation, $dh/dt_0 = -0.02c\omega_\alpha$ ($M = 0.80, \bar{U} = 1.90$, and $\theta = 10.0$).

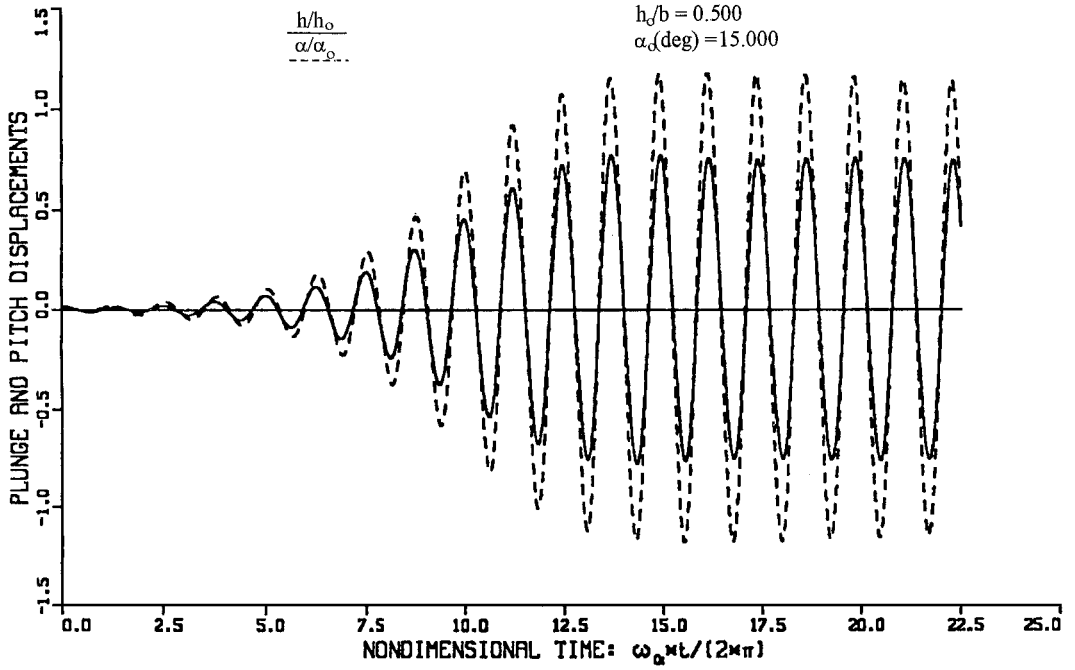

Fig. 8 Limit cycle flutter for the NACA 0012 airfoil without flap and with initial pulse excitations, $\Delta\alpha_0$ = 1.0 deg and $\Delta h_0 = 0.1b$ ($M = 0.85$, $\bar{U} = 4.00$, and $\theta = 75.0$).

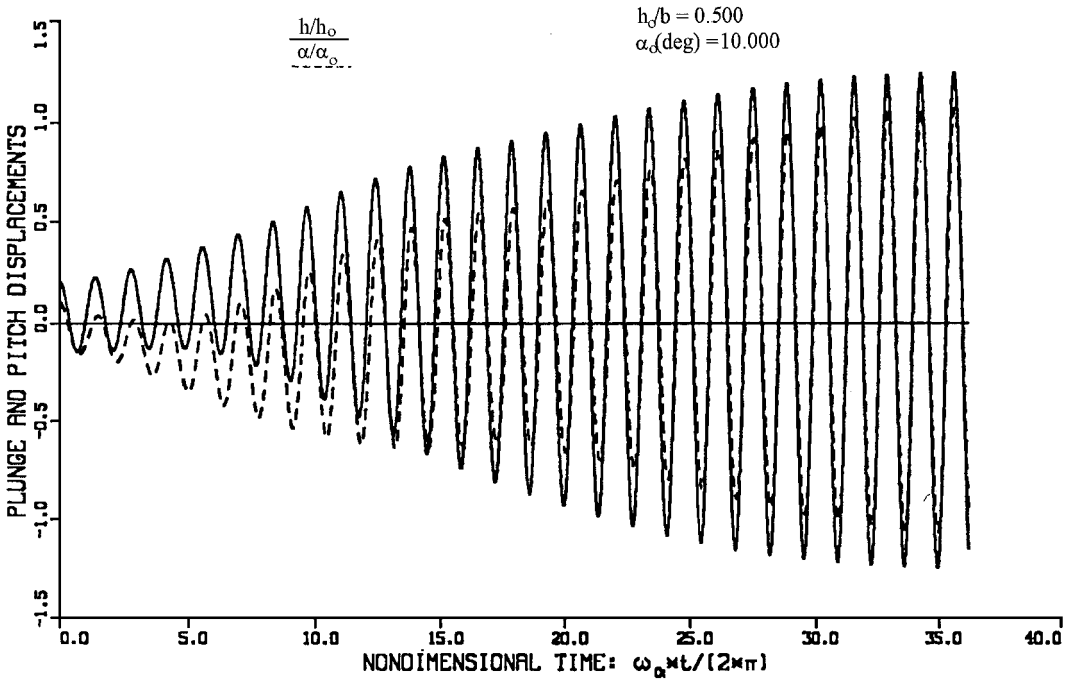

Fig. 9 Weak divergence and flutter–divergence interaction for the NACA 0012 airfoil without flap and with initial pulse excitations, $\Delta\alpha_0$ = 1.0 deg and $\Delta h_0 = 0.1b$ ($M = 0.80$, $\bar{U} = 4.00$, and $\theta = 75.0$).

is depicted in Fig. 10. It shows that the presence of the flap slightly increases the magnitude of the transonic dip. Moreover, the flutter speed was found to decrease again at approximately $M = 0.87$ until $M = 0.89$. This is accounted for by the interaction of the shock waves with the hinge axis. At $M = 0.89$ and at the flutter speed the shock wave was found to move ahead of the hinge, whereas at $M = 0.90$ it remained aft of the hinge. Clearly, this interpretation can be affected by the inclusion of viscous effects, which are neglected in the present study.

The effects of a trailing-edge control surface on limit cycle flutter and weak divergence were also studied in the time domain. Two 3-DOF systems were considered with two different profiles, NACA 0012 and NACA 64A006. Parameters similar to those used in Ref. 15 were selected, and the parameters associated with the flap were, for $c_\beta = 0.5$ (hinge axis at $\frac{1}{4}$ of the trailing edge)

$$x_\beta = 0.008, \qquad r_\beta = 0.06, \qquad \omega_\beta/\omega_\alpha = 1.5$$

All other parameters were identical to those used in generating the results given in Figs. 7–9. At $M = 0.80$, the NACA 0012 airfoil reaches a limit cycle much faster than in the 2-DOF case, using the same initial condition, with flap initially undeflected (see Fig. 11). The amplitude of the limit cycle oscillation in pitch has been reduced by 5%, whereas in plunge it was reduced by more than a half. The weak divergence phenomena still appears at the beginning of the time response, but is quite rapidly quenched by the flutter.

Active Control Studies

Flutter suppression in transonic flow by use of the adaptive controller was studied for both the NACA 0012 and NACA 64A006 airfoils. As in Ref. 16, $[Q]$ is assumed to be the identity matrix. In this study, the output is the vertical acceleration y_k, which is nondimensionalized by multiplying it by a scaling factor, $(100.\, c\gamma/a_\infty^2)$, and subsequently it is filtered by a tenth-order sine-Butterworth filter. With this definition of y_k, a weighting coefficient $r_w = 0.01$ $(1/\text{rad}^2)$ was found to produce good results.

A typical computer simulation of the aeroservoelastic system contains three important time periods. The first 24 sampling steps constitute the learning period. During this period the control surface is activated randomly to obtain initial estimates of the aeroservoelastic system matrices. The maximum random amplitude of the control surface deflection angle is limited to 0.8 deg. At the end of the learning period the controller is engaged and the initial condition for the Ricatti matrix is obtained using Potter's method. In the second period, the active flutter suppression system controls the acceleration at the sensor position, caused by the random control surface motion in the learning period. When the acceleration has been significantly reduced, typically after 48 sampling steps, a perturbation in the angle of attack, the plunge displacement, or plunge and pitch velocities is introduced. In the third period, the active flutter suppression system controls the acceleration at the sensor position caused by this perturbation.

To test the effectiveness of the adaptive controller, a δ function perturbation in plunge velocity equal to $-0.02c\omega_\alpha\,(=-0.04Ma_\infty/\bar{U})$, is introduced at the end of the second period. This nondimensional value was chosen because at $M = 0.85$, $\bar{U} = 3.0$, and $a_\infty = 1100$ ft/s, it is equal to a vertical velocity change of approximately 12.5 ft/s.

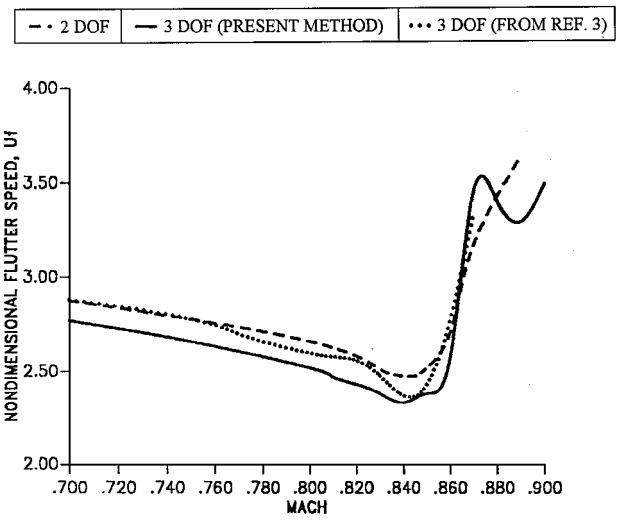

Fig. 10 Effect of flap on flutter speed for a NACA 64A006 airfoil.

Interaction between maximum flap deflection amplitude, deflection rate, and sampling time step was studied first. The NACA 64A006 airfoil, for which the flutter boundary was displayed in Fig. 10, is considered first. At $M = 0.85$, $\bar{U} = 3.0$ is about 20% higher than the flutter velocity. For this unstable flight condition, simulations were carried out using a flap deflection rate, $\mathrm{d}\beta/\mathrm{d}t$, equal to 1.0 deg $a_\infty/(c\sqrt{\gamma})$; thus, with a chord of 10 ft and a freestream speed of sound of 1100 ft/s, $Te_1 \simeq 0.020$ s, one has $\mathrm{d}\beta/\mathrm{d}t \simeq 93$ deg/s. A sampling time step, $Te_1 = 0.4\,\pi/\omega_\alpha$, was considered first. When using the maximum flap deflection $\beta_{\max}$ equal to 4 deg, the active controller failed to suppress flutter as shown in Fig. 12. However, when $\beta_{\max}$ was reduced to 2 deg, the controller successfully suppressed flutter as shown in Fig. 13. This implies that the failure of the controller in Fig. 12 can be attributed to the inability of the actuator to track the variations of the optimal flap deflection angle around the undeflected position. Indeed, the maximum flap deflection angle variation that the actuator model, used in this study, is capable of providing during Te_1 is equal to 1.87 deg. Therefore, at a particular sampling time, when the optimal flap deflection angle is negative and the current flap deflection angle is 4 deg, subsequently, at the next sampling time step, the flap deflection angle will be equal to 2.13 deg, which is far from the desired optimal value. By increasing the sampling time by a factor of two, additional time is provided to the controller, which is sufficient for moving the flap to its optimal position; thus, the controller could suppress flutter even with $\beta_{\max} = 4$ deg, as shown in Fig. 14. These results indicate that the effectiveness of the controller is very sensitive to the ability of the actuator to track variations of the optimal flap deflection angle around the undeflected position.

Effects of shock wave and flow discontinuity due to the presence of the hinge were studied next using the NACA airfoil, for which limit cycle oscillations were shown in Fig. 8. At $M = 0.85$, $\mu = 4.0$, and $\bar{U} = 75.0$, a flutter suppression simulation using $Te_1 = 0.4\,\pi/\omega_\alpha$, $\mathrm{d}\beta/\mathrm{d}t = 1.0$ deg $a_\infty/(c\sqrt{\gamma})$, and $\beta_{\max} = 2$ deg, was

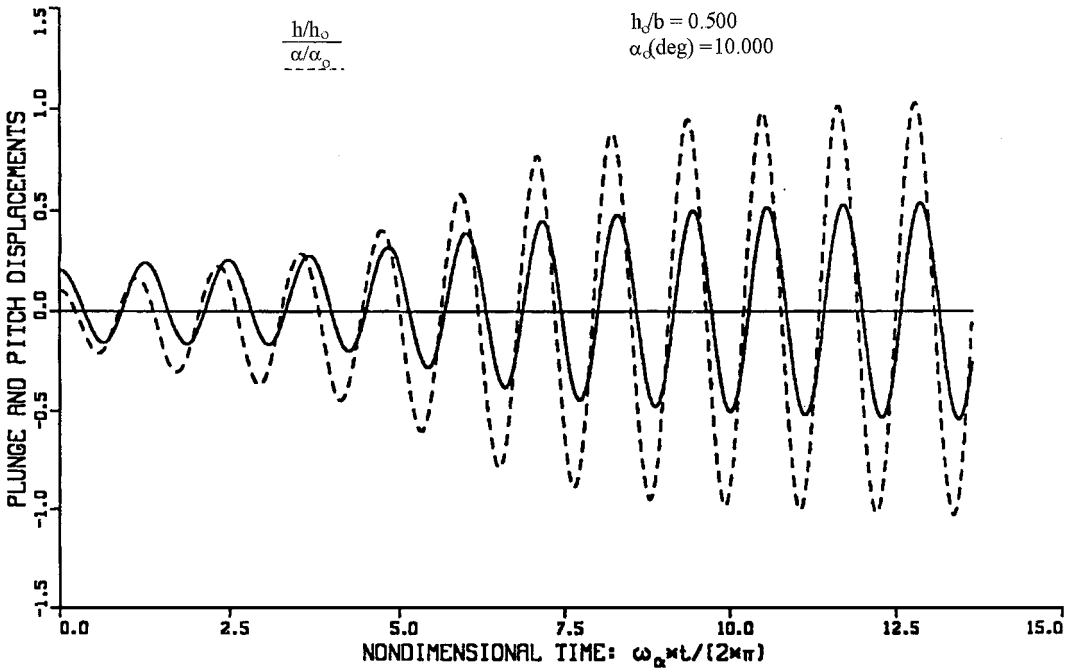

Fig. 11 Effect of flap on weak divergence and flutter–divergence interaction for the NACA 0012 airfoil with initial pulse excitations, $\Delta\alpha_0 = 1.0$ deg and $\Delta h_0 = 0.1b$ ($M = 0.80$, $\bar{U} = 4.00$, and $\theta = 75.0$).

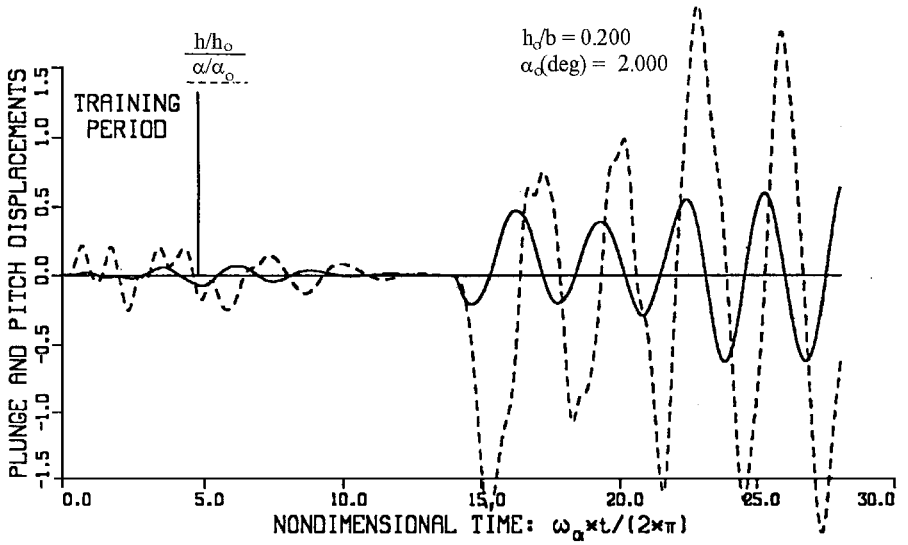

Fig. 12 Time response of the aeroservoelastic system during active flutter suppression with $Te = 0.4\pi/\omega_\alpha$ and $\beta_{max} = 4.0$ deg.

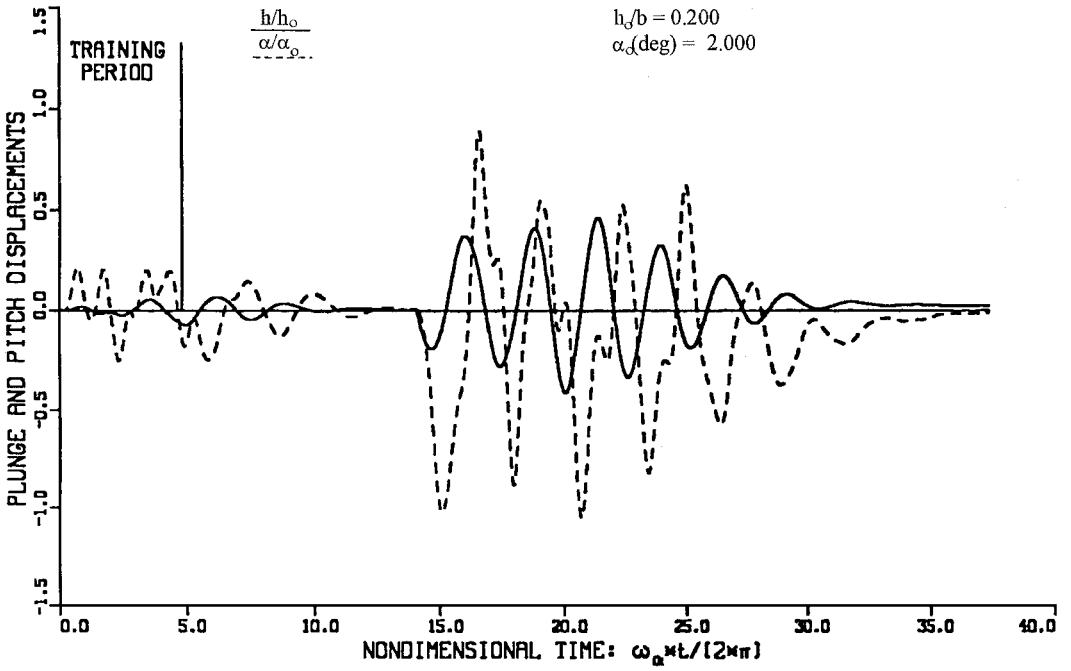

Fig. 13 Time response of the aeroservoelastic system during active flutter suppression with $Te = 0.4\pi/\omega_\alpha$ and $\beta_{max} = 2.0$ deg.

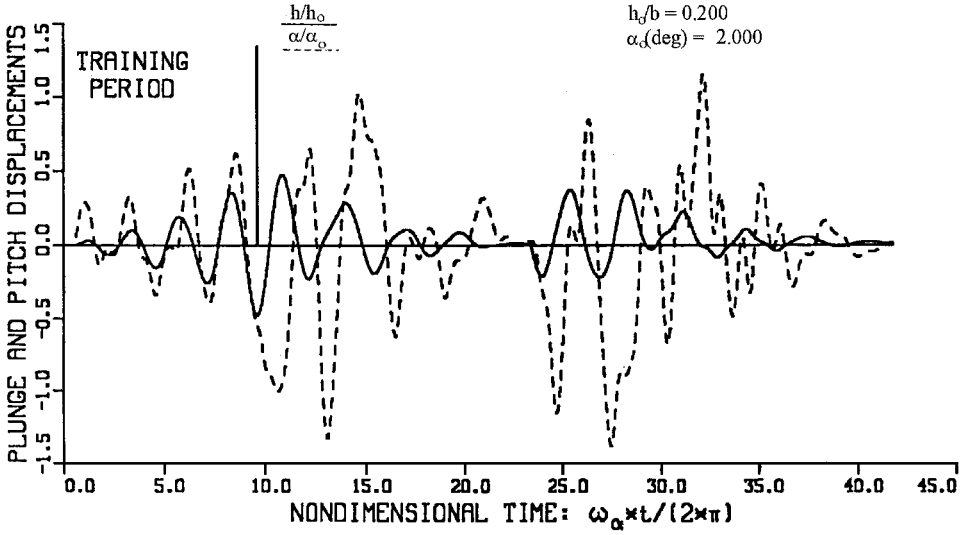

Fig. 14 Time response of the aeroservoelastic system during active flutter suppression with $Te = 0.8\pi/\omega_\alpha$ and $\beta_{max} = 4.0$ deg.

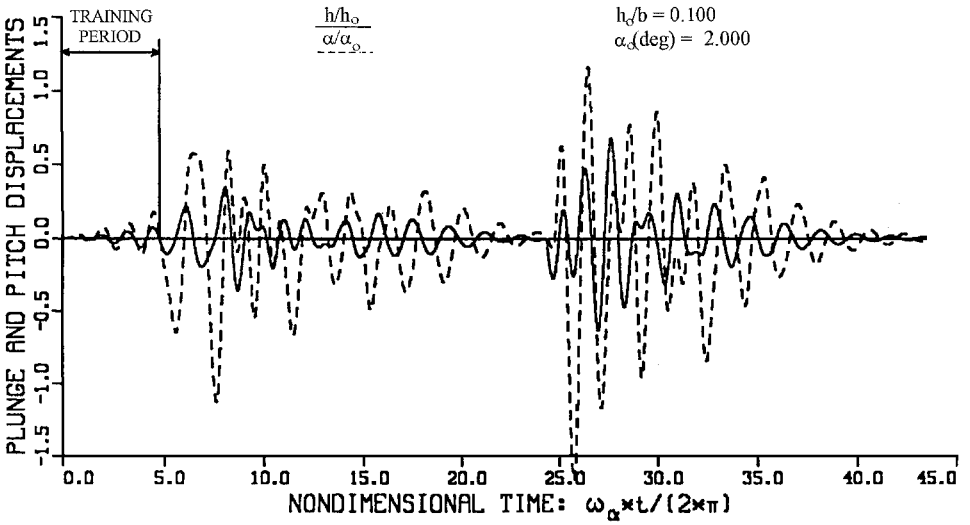

Fig. 15 Time response during active flutter suppression for the NACA 0012 airfoil with hinge axis at 75% of the chord (M = 0.85, $\bar{U}$ = 4.0, and θ = 75.0).

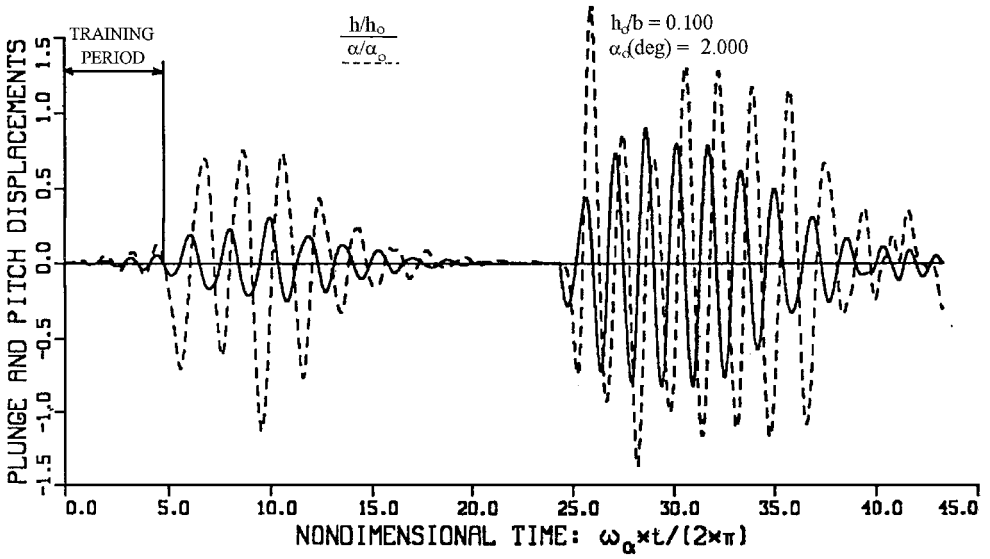

Fig. 16 Time response during active flutter suppression for the NACA 0012 airfoil with hinge axis at 85% of the chord (M = 0.85, $\bar{U}$ = 4.0, and θ = 75.0).

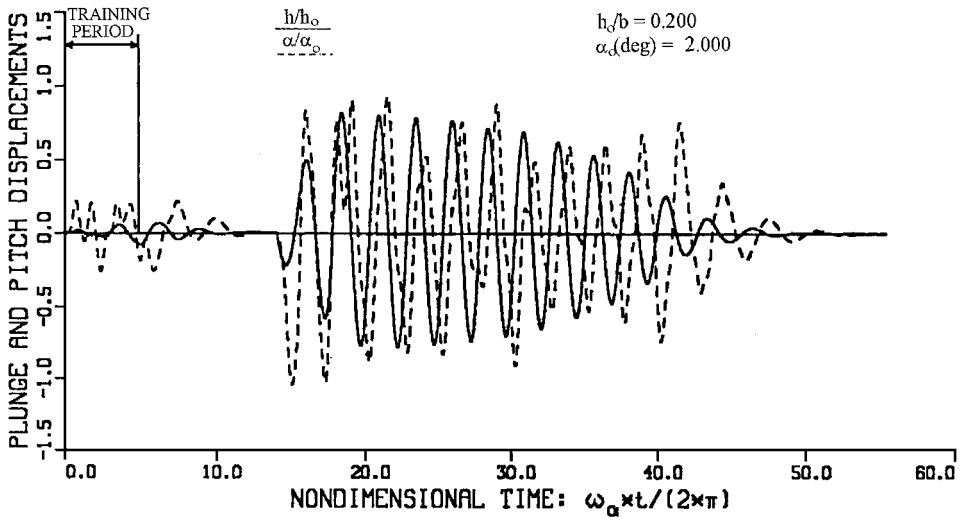

Fig. 17 Effect of the hinge moment correction factor on time response of the aeroservoelastic system during active flutter suppression with δ_h = 0.75, $Te = 0.4\pi/\omega_\alpha$, and β_{max} = 2.0 deg.

carried out. Note from Fig. 15 that the controller successfully suppresses flutter, despite fore and aft shock wave oscillations about the hinge line.

To develop some measure for the flap effectiveness, its influence was studied in two different ways. First, by reducing its length, and second, by using hinge moment correction factors between 0 and 1. Figure 16 depicts the time response of the NACA 0012 airfoil, with the same parameters as those used to compute the time response shown in Fig. 15, except for the hinge axis location, which is moved from 75 to 85% of the chord. Figure 17 depicts the time-response of the NACA 64A006 airfoil, with the same parameters as those for Fig. 13, except for the hinge correction factor, which was reduced to 0.75 instead of 1. Both Figs. 13 and 17 show an increase in the time required to suppress flutter, clearly indicating that flap effectiveness, which can usually be verified only experimentally, plays a significant role.

Conclusions

A two-dimensional aeroservoelastic model combining a 2-DOF airfoil with a trailing-edge control surface was studied. This model, which is based on exact inviscid aerodynamics, can model large amplitude motions and the associated strong shock dynamics. However, the inviscid aerodynamic model used is incapable of capturing shock/boundary layer interactions.

Comparisons between time responses of the open-loop and closed-loop systems show the ability of the trailing-edge control surface to suppress undesirable nonlinear aeroelastic phenomena.

The adaptive controller used here was found to be effective for the nonlinear aeroelastic flutter suppression when the actuator was able to track variations of the flap deflection angle around the undeflected position. In the simulations performed in this study, the adaptive controller effectiveness was found to be robust with respect to changes in the hinge moment correction factor and the hinge axis location.

This study indicates that the synthesis of active flutter suppression systems in the transonic regime requires an integrated approach where CFD-based loads are needed as the basis for the control law design.

This study demonstrates that with the availability of increased computational power and improvement in numerical techniques, aeroservoelastic studies based on unsteady airloads obtained from CFD are becoming feasible.

Acknowledgment

This research was funded by NASA Dryden Flight Research Center under NASA Grant NCC 2-374 provided under the auspices of the University of California, Los Angeles/NASA Dryden Flight Systems Research Center, with K. Gupta as Grant Monitor.

References

[1]Noll, T. E., "Aeroservoelasticity," *Flight-Vehicle Materials, Structures, and Dynamics—Assessment and Future Direction, Vol. 5 Structural Dynamics and Aeroelasticity*, edited by A. K. Noor and S. L. Venneri, American Society of Mechanical Engineers, Fairfield, NJ, 1993, Chap. 3, pp. 179–212.

[2]Friedmann, P. P., "Renaissance of Aeroelasticity and Its Future," *Journal of Aircraft*, Vol. 36, No. 1, 1999, pp. 105–121.

[3]Yang, T. Y., and Chen, C. H., "Transonic Flutter and Response Analyses of Two Three-Degree-of-Freedom Airfoils," *Journal of Aircraft*, Vol. 19, No. 10, 1982, pp. 875–884.

[4]Batina, J. T., and Yang, T. Y., "Application of Transonic Codes to Aeroelastic Modeling of Airfoils Including Active Controls," *Journal of Aircraft*, Vol. 21, No. 8, 1984, pp. 623–630.

[5]Batina, J. T., and Yang, T. Y., "Transonic Time Response of the MBB A-3 Supercritical Airfoil Including Active Countols," *Journal of Aircraft*, Vol. 22, No. 5, 1985, pp. 393–400.

[6]Isogai, K., "The Development of Unsteady Transonic 3-D Full Potential Code and Its Aeroelastic Applications," Paper 17, CP-374, *Transonic Unsteady Aerodynamics and Its Aeroelastic Applications*, AGARD, 1984, pp. 17.1–17.25.

[7]Ide, H., and Shankar, V. J., "Unsteady Full Potential Aeroelastic Computations for Flexible Configurations," AIAA Paper 87-1238, June 1987.

[8]Ide, H., and Ominsky, D., "Simulation of Static and Dynamic Behavior of a Flexible Wing with Multiple Control Surfaces," *Proceedings of the 31st AIAA/ASME/ASCE/AHS/ASC Structures, Structural Dynamics, and Materials Conference*, AIAA, Washington, DC, 1990, pp. 1582–1588.

[9]Guruswamy, G. P., and Tu, E. L., "Transonic Aeroelasticity of Fighter Wings with Active Control Surfaces," *Journal of Aircraft*, Vol. 26, No. 7, 1989, pp. 682–684.

[10]Guruswamy, G. P., "Integrated Approach for Active Coupling of Structures and Fluids," *AIAA Journal*, Vol. 27, No. 6, 1989, pp. 788–793.

[11]Bendiksen, O. O., and Kousen, K. A., "Transonic Flutter Analysis Using the Euler Equations," AIAA Paper 87-0911, April 1987.

[12]Kousen, K. A., and Bendiksen, O. O., "Nonlinear Aspects of the Transonic Aeroelastic Stability Problem," *Proceedings of the 29th AIAA/ASME/ASCE/AHS/ASC Structures, Structural Dynamics, and Materials Conference*, AIAA, Washington, DC, 1988, pp. 760–769.

[13]Guruswamy, G. P., "Time-Accurate Unsteady Aerodynamic and Aeroelastic Calculations of Wing Using Euler Equations," AIAA Paper 88-2281, April 1988.

[14]Robinson, B. A., Batina, J. T., and Yang, H. T., "Aeroelastic Analysis of Wings Using the Euler Equations with a Deforming Mesh," *Proceedings of the 31st AIAA/ASME/ASCE/AHS/ASC Structures, Structural Dynamics, and Materials Conference*, AIAA, Washington, DC, 1990, pp. 1510–1518.

[15]Bendiksen, O. O., "Role of Shock Dynamics in Transonic Flutter," *Proceedings of the 33rd AIAA/ASME/ASCE/AHS/ASC Structures, Structural Dynamics, and Materials Conference*, AIAA, Washington, DC, 1992, pp. 401–414.

[16]Pak, C.-G., Friedmann, P. P., and Livne, E., "Digital Adaptive Flutter Suppression and Simulation Using Approximate Transonic Aerodynamics," *Journal of Vibration and Control*, Vol. 1, No. 4, 1995, pp. 363–388.

[17]Fung, Y. C., *Theory of Aeroelasticity*, Dover, New York, 1969, Secs. 6.10 and 6.11.

[18]Bendiksen, O. O., "A New Approach to Computational Aeroelasticity," *Proceedings of the 32nd AIAA/ASME/ASCE/AHS/ASC Structures, Structural Dynamics, and Materials Conference*, AIAA, Washington, DC, 1991, pp. 1712–1727.

[19]Davis, G., and Bendiksen, O. O., "Unsteady Transonic Euler Equations Using Finite Elements," *Proceedings of the 33rd AIAA/ASME/ASCE/AHS/ASC Structures, Structural Dynamics, and Materials Conference*, AIAA, Washington, DC, 1992, pp. 2203–2213.

[20]Ashley, H., "Role of Shocks in the 'Subtransonic' Flutter Phenomenon," *Journal of Aircraft*, Vol. 17, No. 3, 1980, pp. 187–197.

[21]Rivera, J. A., Dansberry, B. E., Farmer, M. G., Eckstrom, C. V., Seidel, D. A., and Bennett, R. M., "Experimental Flutter Boundaries with Unsteady Pressure Distribution for the NACA 0012 Benchmark Model," *Proceedings of the 32nd AIAA/ASME/ASCE/AHS/ASC Structures, Structural Dynamics, and Materials Conference*, AIAA, Washington, DC, 1991, pp. 697–703.

[22]Jameson, A., Schmidt, W., and Turkel, E., "Numerical Solutions of the Euler Equations by Finite Volume Methods Using Runge–Kutta Time Stepping Schemes," AIAA Paper 81-1259, June, 1981.

[23]Jameson, A., and Baker, T. J., "Solution of the Euler Equations for Complex Configurations," *Proceedings of the AIAA 6th Computational Fluid Dynamics Conference*, AIAA, New York, 1983, pp. 293–302.

[24]Jameson, A., and Schmidt, W., "Some Recent Developments in Numerical Methods for Transonic Flows," *Computer Methods in Applied Mechanics and Engineering*, Vol. 51, 1985, pp. 467–493.

[25]Jameson, A., and Mavriplis, D., "Finite Volume Solution of the Two-Dimensional Euler Equations on a Regular Triangular Mesh," *AIAA Journal*, Vol. 24, No. 4, 1986, pp. 611–618.

[26]Batina, J. T., "Unsteady Euler Airfoil Solutions Using Unstructured Dynamics Meshes," *AIAA Journal*, Vol. 28, No. 8, 1990, pp. 1381–1388.

[27]Magnus, R., and Yoshihara, H., "The Transonic Oscillating Flap," Paper 13, CP-226, *Unsteady Airloads in Separated and Transonic Flows*, AGARD, 1978, pp. 13.1–13.5.

[28]Batina, J. T., "Unsteady Euler Algorithm with Unstructured Dynamic Mesh for Complex-Aircraft Aeroelastic Analysis," *Proceedings of the 30th AIAA/ASME/ASCE/AHS/ASC Structures, Structural Dynamics, and Materials Conference*, AIAA, Washington, DC, 1989, pp. 275–284.

[29]Ballhaus, W., and Goorjian, P., "Efficient Solution of Unsteady Transonic Flows About Airfoils," Paper 14, CP-226, *Unsteady Airloads in Separated and Transonic Flows*, AGARD, 1978, pp. 14.1–14.11.